ADVANCED MATERIALS
www.advmat.de

Regulating Polymer Demixing Dynamics to Construct a Low-Tortuosity Host for Stable High-Energy-Density Lithium Metal Batteries

Gayoung Lee, Dong-Yeob Han, Seongsoo Park, Sangwon Lee, Seungwoo Choi, Seungwon Kim, Youngjin Song, Nam-Soon Choi, Hyun-Wook Lee, Janghyuk Moon, and Soojin Park**

Lithium (Li) metal anodes, despite their exceptional theoretical capacity (3860 mAh g^{-1}), suffer from severe dendrite growth, electrolyte decomposition, and structural instability caused by uneven Li-ion flux and significant volume fluctuations. Here, a one-step, scalable fabrication of 3D hosts that synergistically couple tortuosity modulation with a spatially graded lithiophilicity via precise control of demixing kinetics in a nonsolvent-induced phase separation process is reported. Low-tortuosity (LT) hosts integrate vertically aligned channels for fast ion transport with a silver-gradient interface that directs bottom–up Li deposition, enabling concurrent suppression of dendrites and accommodation of plating-induced volume expansion (4.4% swelling). Finite element simulations confirm the cooperative role of structural alignment in mitigating ion depletion and of chemical gradients in guiding uniform deposition, jointly ensuring stable Li cycling. The LT host sustains >5500 h at 1C in symmetric cells and delivers superior durability in full cells with limited-Li anodes (4 mAh cm^{-2}) paired with $LiFePO_4$ and high-loading $LiNi_{0.8}Co_{0.1}Mn_{0.1}O_2$ cathodes. Double-stacked pouch cells ($N/P = 0.8$, $E/C = 2.5$ g Ah^{-1}) achieve 398.1 Wh kg^{-1} and 1516.8 Wh L^{-1}, retaining 94.2% capacity after 80 cycles. This structural–chemical integration strategy offers a practical, scalable route toward next-generation high-energy-density Li metal batteries.

1. Introduction

The rapid proliferation of electric vehicles (EVs) and portable electronic devices has intensified the demand for high-energy-density rechargeable batteries, positioning lithium (Li) metal as a promising anode candidate due to its extraordinary theoretical capacity (3860 mAh g^{-1}) and the lowest electrode potential (−3.04 V vs SHE).[1] Despite these advantages, the practical application of Li metal batteries (LMBs) is severely impeded by critical challenges: 1) uneven Li-ion flux, inducing localized dendrite formation and internal short circuits; 2) high chemical reactivity of Li leading to continuous electrolyte decomposition; and 3) significant volumetric fluctuations during Li deposition/stripping due to its "hostless" nature, causing structural instability, capacity fading, and safety risks of LMBs.[2]

To address these issues, various strategies have been proposed, including Li surface coatings,[3] separator modifications,[4,5] electric field modulation,[6] and the

G. Lee, S. Lee, S. Park
Department of Battery Engineering
Pohang University of Science and Technology (POSTECH)
Pohang 37673, Republic of Korea
D.-Y. Han, Y. Song, S. Park
Department of Chemistry
Pohang University of Science and Technology (POSTECH)
Pohang 37673, Republic of Korea
E-mail: soojin.park@postech.ac.kr

The ORCID identification number(s) for the author(s) of this article can be found under https://doi.org/10.1002/adma.202510919

DOI: 10.1002/adma.202510919

S. Park, J. Moon
School of Energy Systems Engineering
Chung-Ang University
Seoul 06974, Republic of Korea
E-mail: jhmoon84@cau.ac.kr
S. Choi, H.-W. Lee
School of Energy and Chemical Engineering
Ulsan National Institute of Science and Technology (UNIST)
Ulsan 44919, Republic of Korea
S. Kim, N.-S. Choi
Department of Chemical and Biomolecular Engineering
Korea Advanced Institute of Science and Technology (KAIST)
Daejeon 34141, Republic of Korea

construction of robust artificial solid electrolyte interphases (SEIs) using electrolyte additives,[7,8] high-concentration electrolytes,[9,10] and Fermi-level control.[11] Solid-state electrolytes have also been employed to mechanically suppress dendrite growth.[12,13] While these approaches effectively suppress dendrite growth and electrolyte decomposition, they fail to adequately address the intrinsic volumetric fluctuations of Li, leading to structural instabilities that deteriorate battery performance over prolonged cycling. According to Chazalviel's Sand's time model, Sand's time (τ_{sand}), which represents the onset time of dendritic Li growth caused by cation depletion at the electrode interface, is inversely proportional to the square of the current density ($\tau_{sand} \approx J^{-2}$).[3,14] Based on this principle, researchers have developed 3D conductive frameworks as Li hosts to provide a large surface area, effectively reducing local current density while simultaneously accommodating the volume fluctuations of Li metal during cycling.[4,5,15] However, conventional metallic frameworks significantly compromise the energy density of batteries due to their substantial mass. Additionally, typical 3D hosts frequently exhibit "top-growth" Li deposition due to their high electronic conductivity and limited Li transport at the host surface, leading to uneven Li distribution and elevated risks of dendrite penetration near the separator.

In response, spatial modulation of chemical and structural properties in 3D hosts has emerged as a promising strategy to regulate Li deposition. For example, an electronic conductivity gradient scaffold with conductive Cu nanowires at the bottom and insulating cellulose nanofibers at the top facilitated "bottom–up" growth of Li within the host.[16] Similarly, lithiophilicity gradients using Ag,[17,18] Au,[19] or ZnO[19] which facilitate Li attachment and lower the nucleation overpotential, enable bottom–up Li deposition within the scaffold. Recently, Jiang et al. engineered a hierarchical host with top–down increasing lithiophilicity and conductivity, realizing a synchronous filling mode across the entire framework, exhibiting 3700 h symmetric cycling.[20] In parallel, Zhang et al. reported a dielectric-gradient host constructed by layer-by-layer Sb attenuation. Upon cycling, Sb converts to superionic Li_3Sb, establishing a polarization gradient that pumps Li^+ toward the current collector and sustains 2000 h at 10 mA cm^{-2}.[21] The tortuosity of hosts, a critical parameter governing the complexity of ion transport pathways in porous structures, directly impacts the uniformity of Li-ion flux and Li deposition behavior.[22,23] Low-tortuosity structures have been developed using advanced methods such as heavy ion-tracking,[24] plasma-enhanced chemical vapor deposition,[25] unidirectional freezing,[26] and catalyst-assisted pyrolysis,[27] to decrease ionic resistance and mitigate concentration polarization. However, these techniques often require complex processes, costly equipment, and extended manufacturing times, which limit their scalability for commercial adoption. In contrast, nonsolvent-induced phase separation (NIPS) is an ambient-pressure, roll-to-roll-compatible wet-coating process that tunes pore orientation, porosity, and tortuosity in a single step via solvent-nonsolvent selection.

Herein, we introduce tortuosity-controlled 3D hosts with a lithiophilicity gradient to simultaneously address ionic transport and volumetric expansion challenges in LMBs by regulating polymer demixing dynamics during the NIPS process. The polyacrylonitrile (PAN)-based hosts incorporate single-walled carbon nanotubes (SWCNTs) for electronic conductivity, silver nanoparticles (Ag NPs) as nucleation sites, and an Ag layer on Cu foil for the lithiophilicity gradient. Tortuosity of the hosts was modulated by modulating polymer demixing rates through varying the nonsolvent type during phase separation, yielding three distinct structures: low (LT), moderate (MT), and high tortuosity (HT). Among them, the LT host exhibited superior Li-ion transport and charge transfer properties, enabling uniform and stable Li plating/stripping without dendritic growth. Finite element simulations further reveal that the LT host, with its vertically aligned channels, achieves highly uniform Li-ion distribution and concentrated bottom–up Li deposition, while increased tortuosity in MT and HT hosts induces severe concentration polarization, obstructed ion pathways, and top-favored Li accumulation, corroborating the experimental observations. Asymmetric cells comprised of LT-Li5 (pre-deposited 5 mAh cm^{-2} of Li in LT host) and Li metal (100 μm) demonstrated exceptional cycling stability over 5500 h at 1C with minimal overpotential (<18 mV). Full cells employing the LT–Li4 anode with a $LiFePO_4$ (LFP) cathode exhibited impressive capacity retention of 80% after 350 cycles under challenging conditions with an areal capacity of 2.5 mAh cm^{-2} and a negative-to-positive capacity ratio (*N/P*) of 1.6. Furthermore, a double-stacked pouch-type full cell comprising the LT–Li anode and $LiNi_{0.8}Co_{0.1}Mn_{0.1}O_2$ (NCM811) cathodes (5 mAh cm^{-2}, $N/P = 0.8$) achieved high energy densities of 398.1 Wh kg^{-1} and 1516.8 Wh L^{-1} at a low electrolyte-to-capacity (*E/C*) ratio of 2.5 g Ah^{-1}. This facile electrode fabrication strategy using demixing dynamics, combining tortuosity modulation and a lithiophilicity gradient, enables efficient Li transport, suppresses dendrite formation, and enhances cycling stability, offering practical insights for the design of next-generation high-energy-density LMBs.

2. Results and Discussion

2.1. Preparation of Tortuosity-Controlled Hosts by Regulating Demixing Dynamics

The fabrication of tortuosity-controlled hosts with a lithiophilicity gradient using the NIPS method is schematically illustrated in **Figure 1a**. Compared with traditional 3D-host fabrication (electrospinning, unidirectional freezing, template/chemical vapor deposition, metallic foams), the NIPS process here consolidates pore-architecture formation and lithiophilicity programming into a single coating/immersion step, requires no vacuum or cryogenic equipment, and is compatible with roll-to-roll coating. Initially, PAN and silver nitrate ($AgNO_3$) were dissolved in a cosolvent mixture of *N*, *N*-dimethylformamide (DMF) and N-methyl-2-pyrrolidone (NMP) containing SWCNTs. PAN was chosen as the host matrix owing to its dual role as a robust stabilizer for Ag nanoparticle formation and as a mechanically strong, thermally stable polymer.[28] In addition, the coordination between PAN's nitrile groups and Li^+ ions enhances Li-ion transport and supports efficient, reversible Li plating/stripping.[29,30] The solution was stirred continuously at 70 °C for 12 h to form Ag NPs through DMF-derived Ag-ion reduction (ex situ formed Ag NPs). Subsequently, the PAN–Ag NPs–SWCNT composite solution was cast onto a Cu foil via doctor blading. During casting, residual Ag-ion underwent galvanic reduction at the Cu

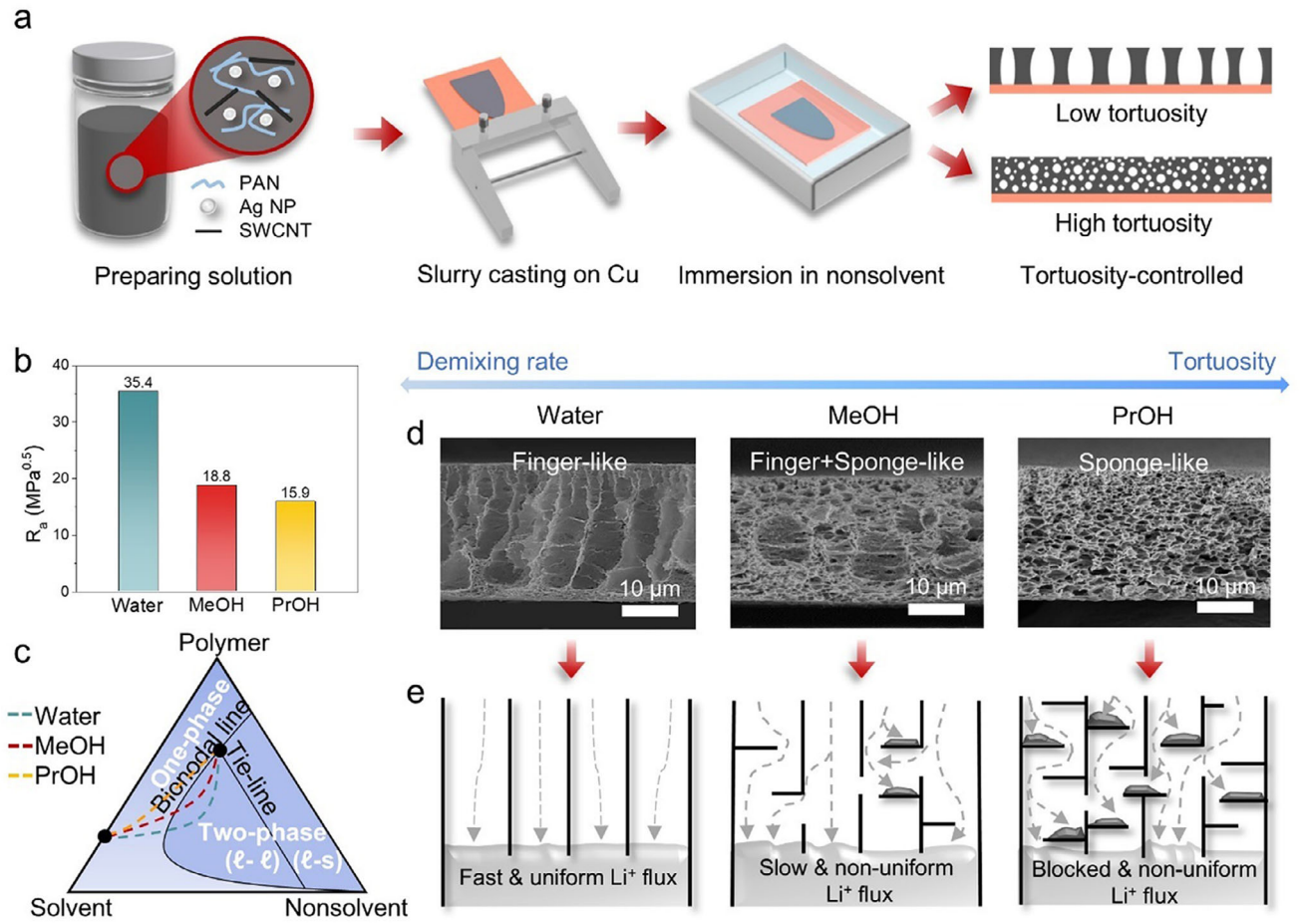

Figure 1. Preparation of tortuosity-controlled hosts. a) Schematic illustration of the fabrication process of hosts through the NIPS technique. b) Calculated Hansen solubility parameter distance (R_a) for selected nonsolvents. c) Ternary phase diagram and composition paths of cast electrodes immediately after immersion (t < 1 s) into different nonsolvents. d) Cross-sectional SEM images of hosts with varying tortuosity. e) Graphical representation illustrating the influence of tortuosity on Li-ion flux distribution and resulting Li deposition behavior.

interface, forming a lithiophilicity gradient (in situ formed Ag layer). The cast film was then immersed in a nonsolvent bath to initiate the NIPS process, during which the cosolvent exchanged with the nonsolvent, inducing phase separation into polymer-rich and polymer-lean domains and yielding a porous structure.

The morphology of the resulting NIPS frameworks is critically dependent on the demixing rate, which can be simply controlled by the choice of nonsolvent. Nonsolvents with low polymer solubility induce rapid demixing, forming finger-like structures characterized by low tortuosity. In contrast, higher-solubility nonsolvents result in delayed demixing and generate sponge-like structures with high tortuosity (Figure S1, Supporting Information). The solubility relationship between the polymer and nonsolvent is quantified using the Hansen solubility parameter distance (R_a), defined in Equation (1):[31]

$$R_a = \sqrt{4\left(\delta_{d,\,P} - \delta_{d,\,NS}\right)^2 + \left(\delta_{p,\,P} - \delta_{p,\,NS}\right)^2 + \left(\delta_{h,\,P} - \delta_{h,\,NS}\right)^2} \quad (1)$$

where δ_d, δ_p, and δ_h represent the dispersion, polar, and hydrogen bonding solubility parameters, respectively, while subscripts "P" and "NS" denote the polymer and nonsolvent. A higher R_a value corresponds to lower polymer solubility, which promotes faster phase separation and the development of finger-like structures.[32] Three representative nonsolvents—water, methanol (MeOH), and propanol (PrOH)—with distinct R_a values were employed (Figure 1b, Table S1, Supporting Information). Water, exhibiting the highest R_a, shows the lowest PAN solubility, whereas PrOH, with the lowest R_a, offers the highest solubility. As illustrated in Figure 1c, immersion in water rapidly shifted the solution into the two-phase region, promoting finger-like morphologies. In contrast, PrOH maintained the system in the single-phase region for a longer duration, leading to delayed demixing and the gradual formation of sponge-like structures upon crossing the binodal boundary.[33,34]

The morphologies of the frameworks prepared with different nonsolvents were characterized by cross-sectional scanning electron microscopy (SEM) images. The water-based host exhibited a distinct finger-like structure with LT due to rapid demixing (Figure 1d). The MeOH-based host showed a hybrid structure of finger-like and sponge-like domains with MT, while the PrOH-based host formed a sponge-like structure with HT due to its slower demixing behavior. Host tortuosity significantly influenced Li deposition behavior (Figure 1e). The LT host enabled fast

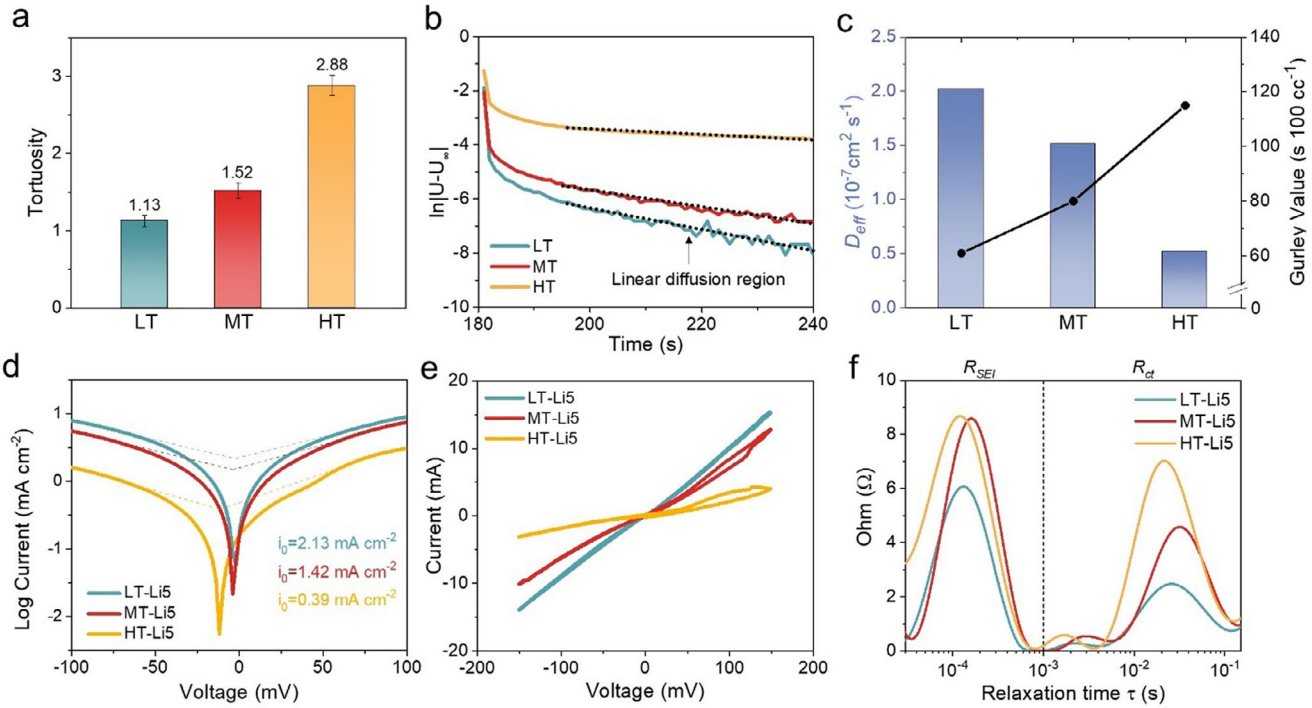

Figure 2. Structural characterization and Li-ion transport properties of hosts. a) Tortuosity values of different hosts calculated using the EIS method. b) $\ln|U(t) - U(t=\infty)|$ versus time (t) plots obtained from the DC polarization/depolarization method. c) Ionic diffusivity values obtained from the DC polarization–depolarization method and Gurley air resistance of hosts with varying tortuosity. d) Tafel plots and e) CV profiles of symmetric cells. f) DRT analysis from EIS measurements of symmetric cells.

and homogeneous Li-ion transport, promoting stable bottom–up deposition, while the HT host restricted ion flux, resulting in surface Li accumulation, hindered internal transport, and increased dendrite formation.

The chemical properties of the hosts were also examined. Under optimized Ag NP synthesis conditions, uniform Ag NPs with an average diameter of 5 nm were obtained, as confirmed by transmission electron microscopy (Figures S2 and S3, Supporting Information). The formation of these ex situ Ag NPs involved the reduction of Ag^+ ions by DMF, a well-established reducing agent at elevated temperature. DMF facilitated the electron transfer to Ag^+ ions, resulting in metallic Ag^0.[35,36] PAN additionally acted as a stabilizer, preventing nanoparticle agglomeration and enabling uniform dispersion within the polymer matrix.[37] Cross-sectional SEM and energy-dispersive X-ray spectroscopy analyses revealed a gradient in Ag content, with 5 wt.% of ex situ formed Ag NPs near the top and 11 wt.% of in situ formed Ag near the Cu interface (Figure S4, Supporting Information). Complementarily, time-of-flight secondary ion mass spectrometry depth profiling (normalized by CN^-) shows Ag^- increasing and AgO^- decreasing with sputter time, evidencing a depth-increasing metallic Ag fraction toward the Cu interface (Figure S5, Supporting Information). These data confirm a through-thickness lithiophilicity gradient that biases Li nucleation to the current collector side. This lithiophilicity gradient effectively guided Li deposition toward the bottom of the host, away from the separator, thereby mitigating dendrite formation and reducing the risk of short circuits.

2.2. Tortuosity Characterization and Ionic Transport Properties of Hosts

The tortuosity (τ) of the prepared hosts was quantified using the electrochemical impedance spectroscopy (EIS) method and following Equation (2):[38]

$$\tau = \frac{\sigma_o}{\sigma_s} \times \varepsilon \tag{2}$$

where σ_0, σ_s, and ϵ represent the intrinsic ionic conductivity, effective ionic conductivity, and porosity, respectively. To obtain the intrinsic ionic conductivity of electrolytes, a specialized cell configuration employing stainless steel (SS) electrodes separated by a polytetrafluoroethylene (PTFE) O-ring was used to eliminate separator interference (Figure S6a Supporting Information).[26] σ_s values were determined from ionic resistance measurements of the respective hosts (Figure S6b, Table S2, Supporting Information). The LT, MT, and HT hosts displayed the ionic resistances (R_{ion}) of 1.61, 2.34, and 6.34 Ω, yielding calculated tortuosity of 1.13, 1.52, and 2.88, respectively (**Figure 2a**). Notably, the LT hosts achieved exceptionally low tortuosity of 1.13, significantly outperforming conventional electrode structure (τ = 3–5).[39,40] The mechanical properties of the hosts were further characterized by tensile stress–strain measurements, revealing a decreasing Young's modulus in order of HT, MT, and LT. This trend reflects the influence of increasing porosity and decreasing tortuosity (Figure S7, Supporting Information). In addition, thermal robustness was benchmarked by thermal shrinkage and

differential scanning calorimetry (DSC) analyses. After 1 h at 150 °C, the LT host exhibited ≈0% areal shrinkage, whereas a PP separator (Celgard 2400) shrank by ≈45% with pronounced curling (Figure S8, Supporting Information). DSC corroborates these results: PP shows a sharp melting endotherm at ≈165 °C, while the PAN-based LT host displays no melting or major endotherms in this range (Figure S9, Supporting Information). A slight baseline drift below ≈115 °C for both films is attributed to moisture release.

A constant current of 1 mA was applied for 100 s to produce a Li-ion concentration gradient in the cell and then allowed to relax until the cell potential approached equilibrium (Figure S10b, Supporting Information). The ionic diffusivity within the hosts was calculated using the slope of the $\ln|U(t) - U(t=\infty)|$ versus t (time, s) plot in the linear ionic diffusion region (Figure 2b; Figure S6c, Supporting Information). A steeper slope in this region indicates a lower restriction of Li-ion movement within the host (calculation details in Table S3, Supporting Information). The calculated ionic diffusivity values demonstrate that the LT host exhibited the highest ionic diffusivity (2.02×10^{-7} cm^2 s^{-1}), followed by the MT host (1.51×10^{-7} cm^2 s^{-1}) and the HT host (5.21×10^{-8} cm^2 s^{-1}) (Figure 2c). Additionally, a Gurley densometer was used to measure the time required for 100 cc of air to pass through each host, providing an indirect assessment of tortuosity by quantifying air resistance. The Gurley value of the LT host (61.4 s) was significantly lower than that of the HT host (114.8 s), attributed to the facilitated airflow through the vertically aligned pores in the host (Figure 2c; Figure S11, Supporting Information).[41]

To evaluate the impact of tortuosity on electrochemical kinetics, symmetric cells were assembled using hosts pre-deposited with 5 mAh cm^{-2} of Li (host–Li5). Tafel analysis showed the highest exchange current density (I_0) for the LT host (2.13 mA cm^{-2}), followed by MT (1.42 mA cm^{-2}) and HT (0.39 mA cm^{-2}), indicating improved interfacial charge transfer with lower tortuosity (Figure 2d).[42] This trend was corroborated by cyclic voltammetry (CV), which showed the LT host with a steep and ideal centrosymmetric CV profile (Figure 2e), reflecting facilitated charge transfer kinetics and highly reversible Li plating/stripping.[42,43] EIS coupled with distribution of relaxation time (DRT) analysis further revealed that the LT host exhibited significantly lower charge transfer resistance (R_{ct}) and impedance of SEI (R_{SEI}). Its optimized pore structure provides facile Li-ion pathways, effectively suppressing ion concentration polarization and thereby reducing R_{ct}. Such efficient and uniform charge transfer behavior further facilitates the formation of a stable SEI layer, as evidenced by the reduced R_{SEI}.[44]

2.3. 3D COMSOL Simulation Results

To further elucidate the impact of electrode tortuosity on Li-ion transport and deposition behavior, a finite element analysis was conducted using COMSOL software. The simulated 3D electrode architectures were validated through tortuosity calculations based on effective diffusion coefficients, yielding 1.00, 1.59, and 2.76 for LT, MT, and HT hosts, respectively, closely matching experimental results and confirming the reliability of the model (Figure S12, Supporting Information). Subsequently, the Li deposition electrochemical reaction of the hosts was incorporated into the simulation model by optimizing Tafel parameters based on the experimentally measured Ag concentration profiles within the hosts. (Figures S13 and S14, Supporting Information). The 3D Li-ion concentration distribution analyses reveal that the LT host achieves uniform Li-ion distribution across vertically aligned channels, minimizing concentration gradients and supporting efficient ion replenishment (**Figure 3a**; Figure S15, Supporting Information). By comparison, the MT and HT hosts display significantly increased concentration polarization as tortuosity rises. The 2D simulation results demonstrate that the LT host provides short and direct pathways for Li-ion diffusion through vertically aligned channels, effectively reducing concentration gradients along the depth of the host. By comparison, the MT host develops partially obstructed Li-ion pathways, while the HT host presents highly tortuous and blocked ion transport channels, ultimately leading to severe ion depletion near the bottom of the host. 3D analyses of local current density further demonstrate that the LT host facilitates high current density at the bottom, driving desirable bottom–up Li deposition (Figure 3b). The MT host, by contrast, shows diminished current density at the bottom and more significant activity in upper regions, while the high tortuosity of the HT host leads to strongly localized current at the top surface, indicating restricted electrolyte penetration. 3D simulated Li deposition profiles quantitatively illustrate these effects (Figure 3c). The LT host yields a clear bottom–up growth pattern, with maximal deposition near the current collector (0.77 µm) and less at the top (0.47 µm). The MT host displays lower bottom deposition (0.70 µm, −6.7% vs LT) and increased top deposition (0.61 µm, +35.6% vs LT) with a significant disparity, indicating the onset of non-uniform, top-favored Li growth. For the HT host, Li predominantly accumulates at the top (0.79 µm), with minimal deposition at the bottom (0.33 µm), suggesting Li accumulation at the host surface and inefficient host utilization. To isolate porosity effects from tortuosity, we further conducted a parametric COMSOL study in which tortuosity was varied from 80% to 50% while fixing the LT geometry and tortuosity of 1.13. Across this range, the plating remained bottom-biased, although decreasing porosity intensified concentration polarization and modestly reduced the bottom-deposition fraction (Figure S16, Supporting Information). Collectively, these simulation results underscore the critical importance of low tortuosity combined with a spatially engineered lithiophilicity gradient in enabling facile and uniform Li-ion transport and bottom–up Li metal deposition.

2.4. Influence of Tortuosity on Li Plating Morphology and Reversibility

Building on the insights from 3D simulation results, we systematically investigated the experimental reversibility of Li plating and stripping in hosts with varying tortuosity (Figure 3a). The LT host exhibited highly uniform Li deposition with an approximate thickness of 25 µm after 5 mAh cm^{-2} of Li plating (ideally 5 µm per 1 mAh cm^{-2} Li), indicating dense, bottom–up deposition without surface Li accumulation (**Figure 4a**). In contrast, the MT host displayed non-uniform and partial plating, while the HT host exhibited significant top plating, as further corroborated by top-view SEM images (Figure S17, Supporting Information).

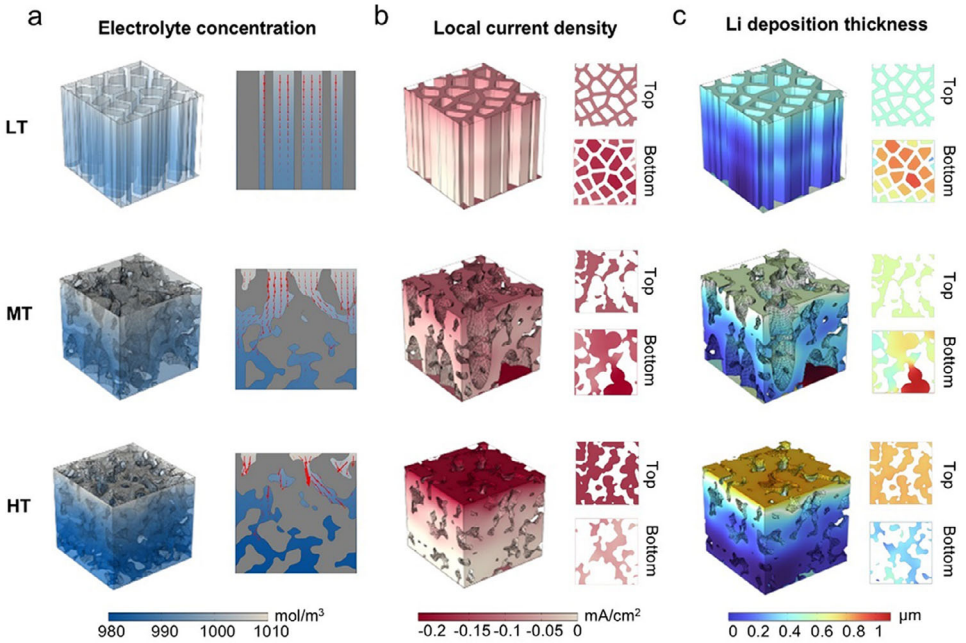

Figure 3. 3D COMSOL simulation results. a) Li-ion concentration distributions in LT, MT, and HT host structures. b) Local current density contour plot at the level of the electrode and current collector. c) Deposited Li metal thickness distribution across electrode regions.

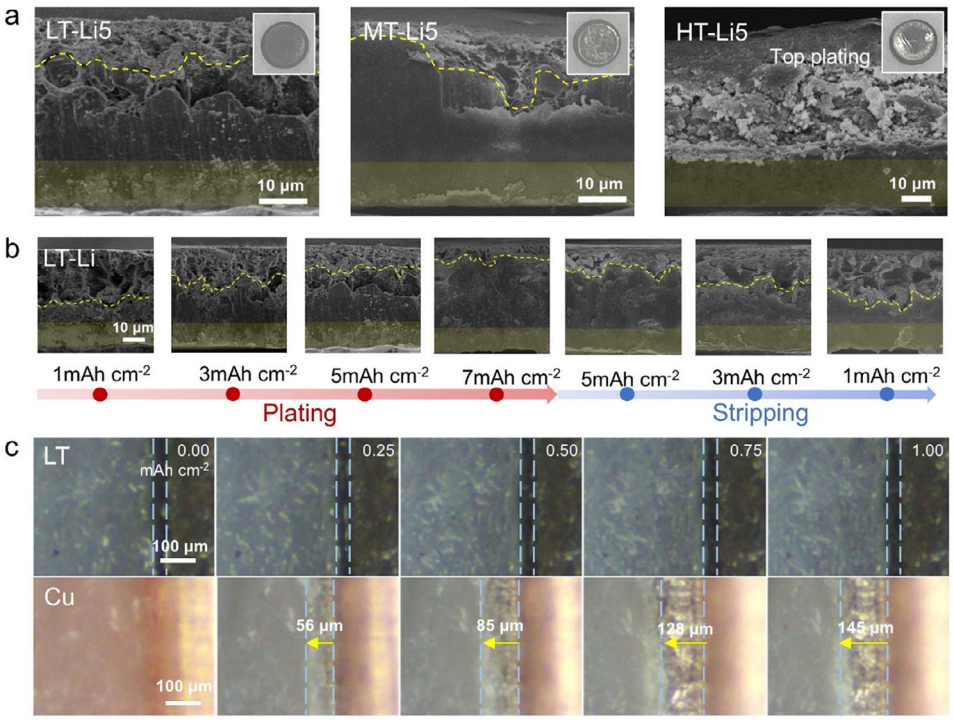

Figure 4. Li deposition and stripping morphology in the hosts. a) Cross-sectional SEM images of different hosts after Li plating (5 mAh cm^{-2}) (Insets: Digital photos of hosts after Li plating). b) Cross-sectional SEM images of the LT host at different states of Li deposition and stripping stages. c) In situ OM analysis of Li deposition on LT host and Cu foil (1 mAh cm^{-2}, 0.5 mA cm^{-2}).

These observations emphasize that reduced tortuosity markedly facilitates efficient Li-ion transport, thereby ensuring dense Li deposition within the host structure.

Cross-sectional SEM analyses further explored the reversibility of Li deposition and stripping within the LT host (Figure 4b). Initially, Li predominantly deposited near the host bottom region, progressively occupying upper regions with increasing Li deposition, verifying the bottom–up deposition mechanism. During stripping, Li removal proceeded from the top to the bottom, underscoring excellent reversibility. X-ray diffraction provided additional evidence of reversibility by tracking Ag alloying-dealloying behavior during cycling (Figure S18, Supporting Information). Initially, the Ag (111) peak appeared at 38.3°, shifted slightly upon Li alloying to form Ag_3Li_{10} after Li deposition, and subsequently recovered after stripping, confirming reversible interactions between Li and Ag.[45]

In situ optical microscopy (OM) was performed under low external pressure conditions (≈0.2 MPa) at a current density of 0.5 mA cm^{-2} to highlight the practical advantages of the LT host.[46] Under identical conditions, the bare Cu electrode exhibited porous, significantly expanded Li deposition with a thickness of ≈150 µm after depositing 1 mAh cm^{-2} of Li due to the "host-less" nature of Li (Figure 4c; Figure S19, Supporting Information). In sharp contrast, no significant volumetric expansion was observed within the LT host under identical conditions. These results validate the synergistic effectiveness of lithiophilicity gradients combined with low-tortuosity structures in facilitating stable, dense Li deposition, even under low external mechanical pressure. Complementarily, DSC analyses were performed on Li plated on bare Cu and Li plated within the LT host to assess safety-relevant thermal behavior. The LT architecture delays the onset and reduces the post-melting exothermic heat release to 4367.3 J g^{-1}, compared to 5133.9 J g^{-1} for Li on Cu (Figure S20, Supporting Information). The diminished heat output is consistent with denser, lower-surface-area Li formed within the low-tortuosity scaffold, which suppresses parasitic reactions during thermal excursion.[47] These results indicate that the LT host raises the thermal safety margin of Li metal anodes under practical operating conditions.

2.5. Cycling Stability of Tortuosity-Controlled Hosts

Considering the differences in Li transfer kinetics and deposition behavior induced by electrode structure, we confirmed that tortuosity directly impacts electrochemical performance during cycling. To evaluate Li-ion transport, we combined the galvanostatic intermittent titration technique (GITT) with galvanostatic cycling in symmetric cells (Figure S21, Supporting Information).[48] GITT, which applies current pulses followed by relaxation periods, allows Li-ion concentration gradients to equilibrate, thereby reducing concentration-induced polarization. The LT host showed minimal voltage deviation between the two methods, indicating efficient ion transport through vertically aligned channels. In contrast, the HT host exhibited a significantly higher overpotential during galvanostatic cycling than during GITT, reflecting hindered ion transport due to high tortuosity.

Galvanostatic cycling was carried out on asymmetric cells pairing a host-Li5 working electrode with a 100 µm-thick Li foil reference/counter electrode to examine Li deposition and stripping behaviors under various conditions. This asymmetric configuration was adopted to evaluate cell failure intrinsically induced by host structure degradation. In rate performance tests, the LT host exhibited stable voltage profiles and low overpotentials of 13, 24, 30, and 45 mV at 1C, 2C, 3C, and 5C, respectively, indicating superior Li-ion transport kinetics and interfacial stability (**Figure 5a**; Figure S22, Supporting Information). In contrast, the HT host showed increasing overpotentials and unstable voltage profiles with rising current density, reflecting poor ion transport and non-uniform Li deposition. Similarly, when cycled at a high current density of 5C, the LT host maintained stable operation for over 600 h with low polarization (≈20 mV), whereas the MT and HT hosts exhibited rapid overpotential increases after only 170 and 25 h, respectively (Figure 5b). The bare Cu electrode, owing to its lithiophobic surface and limited electroactive area, displayed a high overpotential of 80 mV and failed within 15 h (Figure S23, Supporting Information).

At a moderate cycling condition (1C, 0.5 mAh cm^{-2}), the LT host exhibited exceptional cyclability, maintaining stable voltage profiles for over 5500 h without signs of degradation (Figure 5c). In contrast, the HT host failed within 1000 h due to severe polarization caused by dead Li accumulation and electrolyte depletion, driven by continuous Li top-growth and parasitic reactions. At an increased areal capacity of 2 mAh cm^{-2}, the LT host sustained stable operation for over 1200 h, while the MT and HT hosts exhibited early voltage fluctuations (Figure S24, Supporting Information). Remarkably, even at a high capacity of 4 mAh cm^{-2}, corresponding to a Li utilization ratio of ≈80%, the LT host maintained cycling stability for 600 h. Such excellent reversibility of Li plating and stripping, enabled by its low-tortuosity, lithiophilic gradient structure, allows for reduced *N/P* ratios in full cell configurations, thereby maximizing the overall energy density of LMBs.

To further clarify the dynamic interfacial kinetics during cycling, in situ galvanostatic EIS (GEIS) combined with DRT analysis was conducted on asymmetric cells during the plating process after 100 cycles (Figure 5e). The results revealed that the LT host exhibited the lowest SEI and R_{ct} throughout the deposition process, while the MT and HT hosts showed significantly higher resistances, particularly notable in their abrupt R_{ct} increases toward the end of plating. This abrupt increase in R_{ct} for MT and HT is attributed to the progressive ion depletion and subsequent polarization near the host surface, driven by their higher structural tortuosity. In addition, the HT host also shows a marked increase in R_{SEI} during Li plating, resulting from surface Li accumulation and subsequent parasitic reactions with the electrolyte. Collectively, these electrochemical results underscore the pivotal role of low tortuosity in enabling enhanced Li-ion transport, homogenous Li deposition, and significantly improved cycling stability.

The electrochemical performance of the LT host without Ag incorporation was also evaluated to confirm the beneficial impact of the Ag-induced lithiophilicity gradient. Comparative voltage profiles revealed substantially lower nucleation overpotentials for the Ag-containing LT host (8 mV) compared to the Ag-free counterpart (33 mV), highlighting the efficacy of Ag in reducing the Li nucleation barrier through enhanced Li affinity (Figure S25, Supporting Information). Correspondingly, Tafel analysis of the Ag-free LT host yielded a reduced exchange current density

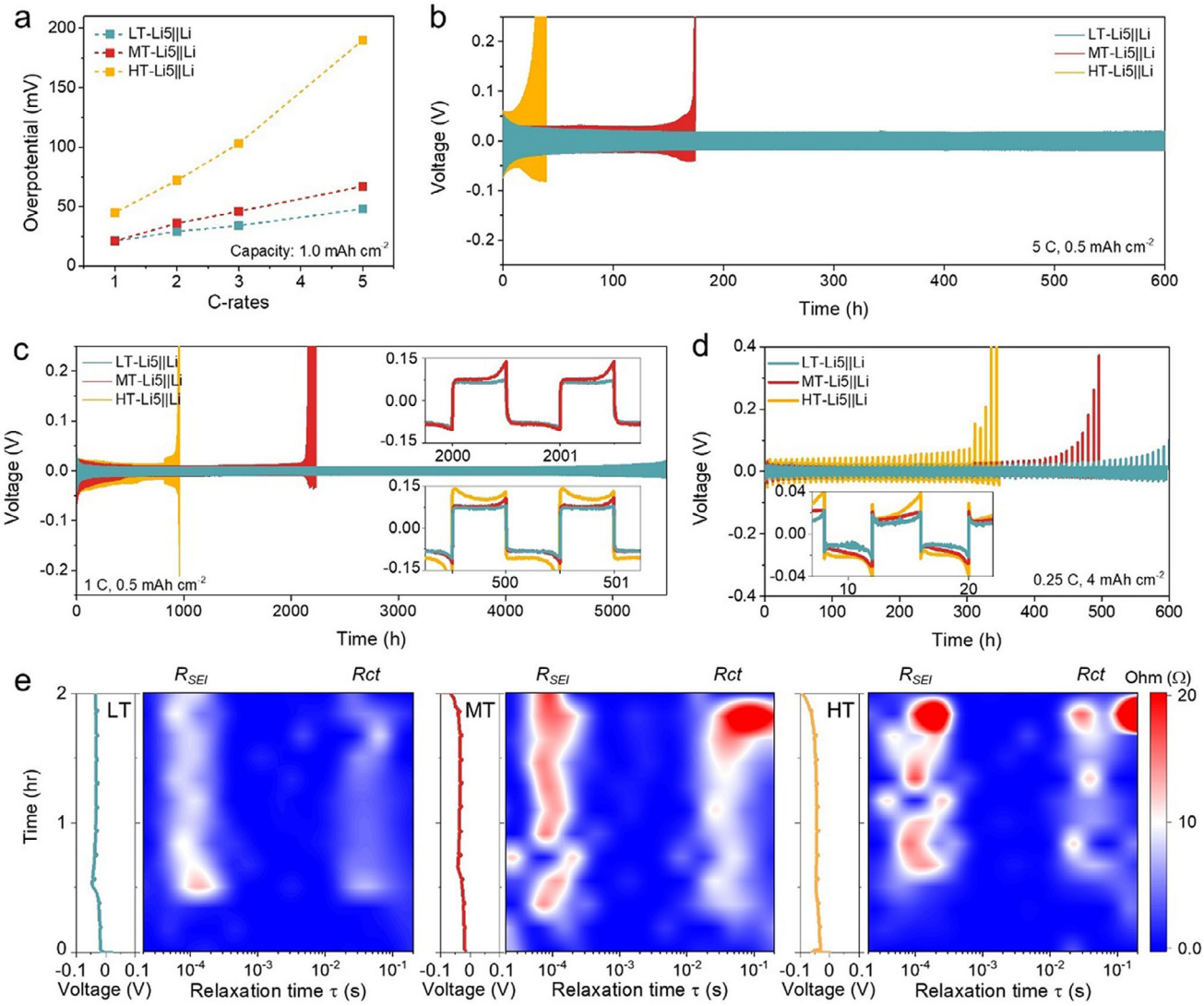

Figure 5. Cycling performance of different hosts. a) Rate performance of asymmetric host-Li5||Li cells at various current densities from 1C to 5C with a fixed capacity of 1 mAh cm^{-2}. b) Long-term cycling performance of host-Li5||Li cells at 5C with 0.5 mAh cm^{-2}. c) Long-term cycling performance of host-Li5||Li cells at 2C with 0.5 mAh cm^{-2} (Inset: Enlarged voltage profiles at certain cycles). d) Long-term cycling stability of host-Li5||Li cells at 0.25C with 4 mAh cm^{-2}. (Inset: Enlarged voltage profiles at certain cycles). e) In situ GEIS-DRT analysis of host-Li5||Li cells during Li plating.

(I_0 = 1.13 mA cm^{-2}), substantially lower than the Ag-containing LT host (I_0 = 2.13 mA cm^{-2}), further confirming the critical role of Ag in facilitating efficient and stable charge-transfer processes (Figure S26, Supporting Information).

2.6. Post-Mortem Analysis of Structural and Interfacial Stability

Post-mortem analysis of hosts was conducted on asymmetric cells after 100 cycles to evaluate host durability after prolonged cycling. Cross-sectional SEM images showed minimal thickness increase (4.4%) in the LT host, indicating excellent structural retention (**Figure** 6a), whereas the MT and HT hosts showed 17.8% and 31.1% expansion, respectively, due to progressive Li top plating (Figure 6b). The bare Cu electrode displayed highly porous, dendritic Li deposition accompanied by drastic thickness expansion (≈420%, Figure S27, Supporting Information).

Interfacial stability was investigated using X-ray photoelectron spectroscopy (XPS) to analyze the SEI formed on cycled asymmetric cells (Figure 6c). The SEI composition varied significantly with host tortuosity. As tortuosity increased from LT to HT, the carbon atomic ratio in the SEI rose markedly, indicating intensified electrolyte decomposition. Top plating on the HT host induced continuous SEI fracture and reformation, leading to a thick, organic-rich SEI layer. In contrast, XPS spectra of the LT host showed stronger F 1s and N 1s peaks with a high content of LiF and Li_3N (Figure 6d,e),[49] reflecting enrichment in inorganic species due to stable inward Li deposition facilitated by the low-tortuosity structure. The polar nitrile groups in PAN strongly adsorb anions, which decompose with the assistance of electron-rich Ag–Li alloys to form an anion-derived SEI layer.[50]

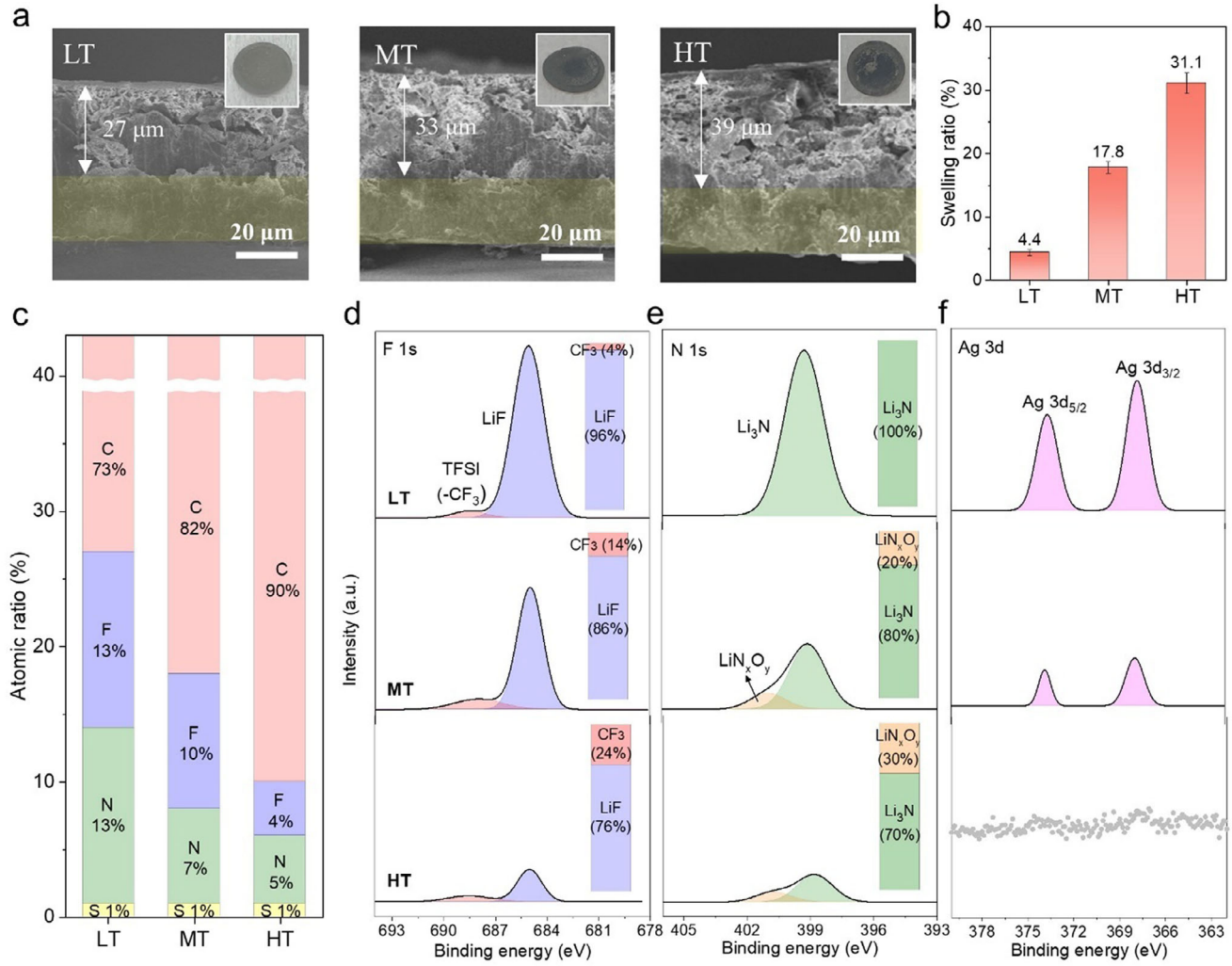

Figure 6. Post-mortem structural and chemical analysis. a) Cross-sectional SEM images and b) swelling ratio of hosts after 100 cycles (Insets: Digital photos of cycled electrodes). c) Atomic concentration analysis of carbon (C), fluorine (F), nitrogen (N), and sulfur (S) at host surfaces obtained from XPS after cycling. XPS spectra of d) F 1s, e) N 1s, and f) Ag 3d (Insets: relative composition of SEI components corresponding to each element).

This mechanism was supported by linear sweep voltammetry, which revealed more pronounced $LiNO_3$ decomposition peaks on the LT host compared to bare Cu (Figure S28, Supporting Information). Furthermore, Ag 3d signal intensity inversely correlated with tortuosity, suggesting thinner SEI formation and greater Ag exposure on the LT host surface, while the HT host exhibited suppressed Ag signals due to thick SEI formation driven by repeated top plating and uncontrolled electrolyte breakdown (Figure 6f). The bare Cu electrode showed even higher organic SEI content than the HT host, attributed to dendritic Li growth that continuously exposed fresh Li surfaces to electrolyte degradation (Figure S29, Supporting Information). Continuous growth of the SEI and electrolyte decomposition during calendar aging remain critical challenges for LMBs, primarily due to the high reactivity of Li. Inorganic-rich SEI layers with high mechanical robustness and electronic insulation effectively suppress electrolyte degradation over prolonged storage. To evaluate interfacial stability, the overpotential and interfacial resistance of asymmetric cells using the LT or bare Cu electrode were compared before and after a two-day rest period (Figure S30, Supporting Information). The LT host exhibited negligible changes in both parameters, indicating the formation of a stable, inorganic-rich SEI, whereas the Cu electrode showed significant increases, suggesting ongoing SEI decomposition due to its unstable, organic-rich nature.

Quantitative evaluation of electrolyte decomposition was performed using ^{19}F nuclear magnetic resonance (^{19}F NMR) spectroscopy by monitoring the concentration of bis(trifluoromethanesulfonyl)imide ($TFSI^-$) anions, originating exclusively from the LiTFSI salt (details provided in Experimental Section, Supporting Information). After 100 cycles, bare Cu cells consumed nearly three times more Li salt than LT cells (Figure S31, Supporting Information), indicating severe electrolyte depletion from repeated SEI regeneration caused by uncontrolled dendritic Li growth. These findings underscore the critical role of host architecture in maintaining electrolyte stability and cycling performance.

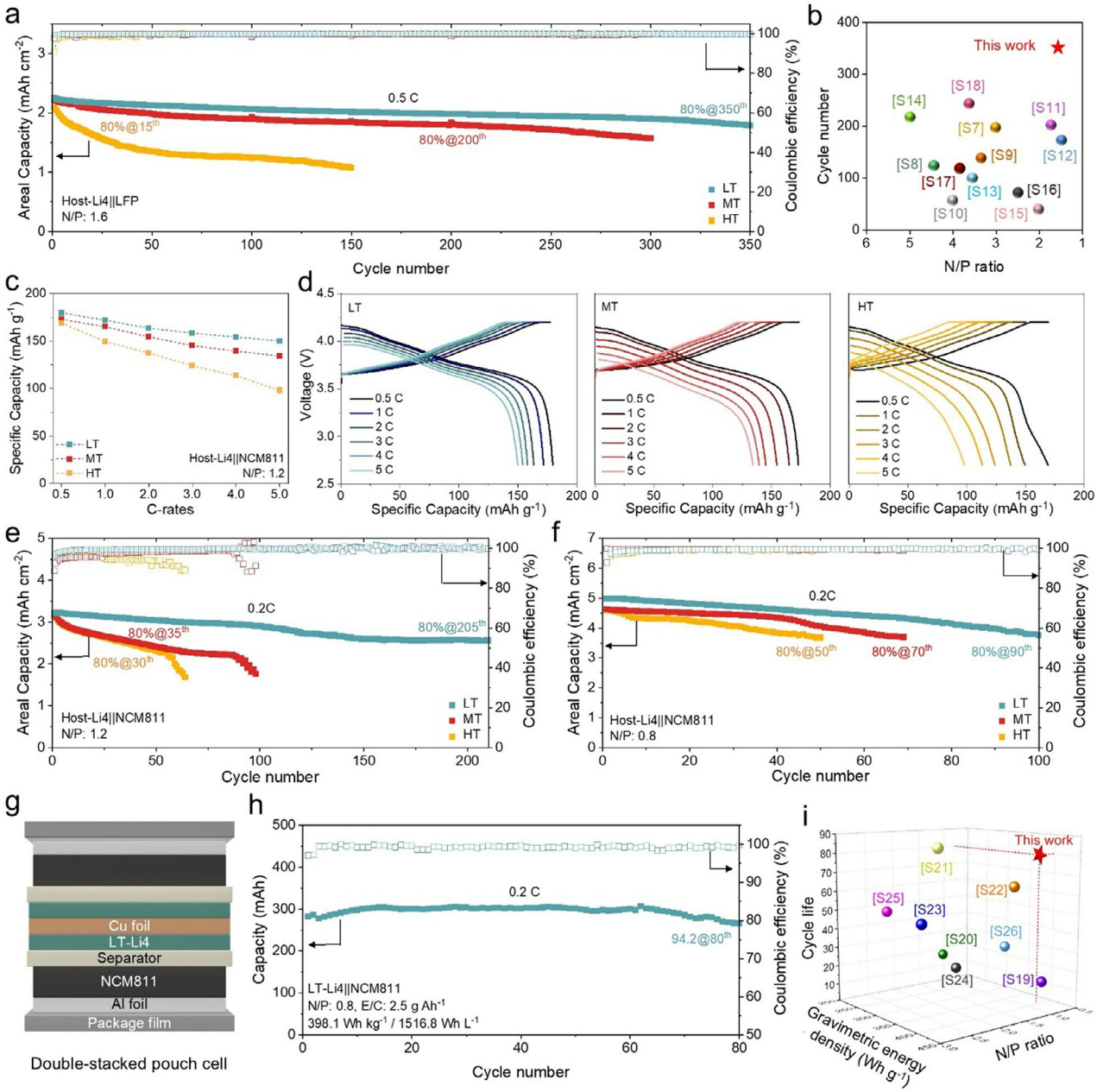

Figure 7. Practical full cell performance of host-Li4 anodes. a) Long-term cycling performance of host-Li4||LFP full cells. b) Comparison of cycling performance for LT-based full cells with previously reported Li metal full cells with a low *N/P* ratio. c) Rate capability and d) corresponding voltage profiles of host-Li4||NCM811 at varied current densities. Cycling performance of host-Li4||NCM811 full cells with an *N/P* ratio of e) 1.2 and f) 0.8. g) Configuration schematic of double-stacked pouch-type full cell incorporating the LT host. h) Cycling performance of the double-stacked pouch-type full cell. i) Comparison of the pouch cell performance in this work with previously reported pouch-type Li metal full cells with a low *N/P* ratio.

2.7. Practical Validation of Hosts in Full Cells

The practical applicability of the developed hosts was assessed by pairing Li pre-deposited host-Li4 anodes with LFP and NCM811 cathodes in coin-type full cells. A limited Li amount of 4 mAh cm^{-2} was used to achieve low *N/P* ratios, thereby assessing performance under stringent conditions. In long-term cycling of host-Li4||LFP full cells with an areal capacity of 2.5 mAh cm^{-2}, LT host demonstrated superior durability, retaining 80% of its capacity after 350 cycles, significantly outperforming the MT and HT cells (**Figure** 7a). The rapid degradation in the HT-Li4||LFP cell was attributed to Li accumulation on the host surface due to restricted ion transport. Similarly, the Cu-Li4||LFP cell showed an accelerated capacity loss from dendritic growth and dead Li formation (Figure S32, Supporting Information). Notably, the LT-Li4||LFP full cell outperformed previously reported LMBs with low *N/P* ratios (<5), highlighting the superior stability of the LT host (Figure 7b, Table S4, Supporting Information).

Post-cycling characterization was also conducted after 100 cycles using SEM and XPS analyses. Cross-section SEM images show that LT retains a dense, bottom–up Li inventory confined within the framework without top plating, whereas MT and HT exhibit surface Li crusts indicative of repeated top-growth (Figure S33, Supporting Information). XPS of the cycled hosts reveals that LT forms an inorganic-rich SEI with higher fluorine content and lower surface Li fraction compared to MT and HT, consistent with confined deposition without top plating (Figure S34, Supporting Information).

To further enhance energy density, host-Li4 anodes were paired with NCM811 cathodes, which offer higher specific capacity (≈200 mAh g^{-1}) and operating voltage (≈3.7 V vs Li/Li^+) than LFP cathodes (≈170 mAh g^{-1}, ≈3.4 V).[51] In Figure 7a–e, the NCM811 cathodes had a mass loading of 17.5 mg cm^{-2} (N/P = 1.2), whereas Figure 7f,h correspond to high-loading cathodes of 25 mg cm^{-2} (N/P = 0.8). Rate capability tests confirmed the superior performance of the LT-Li4||NCM811 cell, which delivered discharge capacities of 173, 165, 160, 155, and 149 mAh g^{-1} at current densities of 0.5C, 1C, 2C, 3C, and 5C, respectively (Figure 7c; Figure S35, Supporting Information). Especially at 5C, the LT-based cell achieved a capacity 1.5 times higher than that of the HT-based cell. Moreover, the LT host exhibited a more gradual increase in overpotential with increasing C-rate, indicating that the low-tortuosity structure of the host effectively enhances Li reaction kinetics (Figure 7d). High-areal-capacity NCM811 cathodes (3.3 and 5 mAh cm^{-2}) were paired with host-Li4 anodes, corresponding to N/P ratios of 1.2 and 0.8, to demonstrate practical feasibility under demanding conditions. At an N/P ratio of 1.2, MT and HT cells exhibited rapid capacity fading within 88 and 53 cycles, respectively, primarily due to irreversible Li deposition and stripping inside the hosts, while still outperforming Cu-based cells (Figure 7e; Figure S36, Supporting Information). In contrast, the LT-Li4||NCM811 cell showed stable cycling with 80% capacity retention after 205 cycles (Figure 7e). Under more stringent conditions (N/P = 0.8), the LT-based full cell maintained 80% retention for up to 90 cycles, surpassing MT and HT cells, which reached this threshold at 70 and 49 cycles, respectively (Figure 7f).

Scalability and practical implementation were demonstrated by fabricating a double-stacked pouch cell with LT-Li4 anodes and NCM811 cathodes at an N/P ratio of 0.8 and E/C ratio of 2.5 g Ah^{-1}, maximizing energy density (Figure 7g). These pouch cells delivered 306.6 mAh capacity with a high energy density of 398.1 Wh kg^{-1}/1516.8 Wh L^{-1} (excluding package materials), enabled by the lightweight polymer host (Figure S37, Table S5, Supporting Information). They also exhibited excellent cycling stability, retaining 94.2% capacity after 80 cycles at 0.2C, confirming the effectiveness of the LT host with tailored lithiophilicity gradients for stable, high-energy-density LMBs (Figure 7h). Moreover, thermal safety was assessed on the 0.3 Ah pouch cells using accelerating rate calorimetry with a heat-wait-seek protocol (Figure S38, Supporting Information). The LT-Li4||NCM811 pouch cell showed a thermal runaway (T_{TR}) temperature of 156 °C, 34 °C higher than the Cu-Li4||NCM811 control, reflecting the dimensional stability of the LT host and confined bottom–up Li deposition, which suppresses the parasitic side reactions upon heating (well-consistent with Li plating DSC).[52] Comparison with recent pouch-type LMB studies featuring low N/P ratios (<3) highlights the superior gravimetric energy density and cycle life of the LT host-based pouch cell, underscoring its potential for practical application in high-energy-density battery systems (Figure 7i, Table S6, Supporting Information). Beyond the double-stacked 0.3 Ah pouch cells, we further scaled the process to large-area LT films (10 cm × 11 cm) prepared by NIPS casting. An Ah-level pouch cell was assembled using five double-sided NCM811 cathodes and a balanced stack of four double-sided plus two single-sided LT-Li4 anodes (N/P = 1.2). The cell delivered 0.97 Ah and showed stable cycling over 20 cycles (Figure S39, Supporting Information), confirming that the low-tortuosity/lithiophilicity-gradient architecture and the Li pre-deposition step translate to large-format assembly.

3. Conclusion

In summary, we have successfully demonstrated a facile and scalable approach to fabricate tortuosity-controlled 3D hosts via regulated polymer demixing dynamics during the NIPS process, integrating spatially modulated lithiophilicity gradients. The optimized LT host, featuring a vertical pore structure with a tortuosity of 1.13, significantly enhances Li-ion transport kinetics, promotes homogeneous bottom–up Li deposition, and effectively accommodates volumetric fluctuations. Finite element simulations further corroborate these findings, revealing that the LT host achieves highly uniform Li-ion distribution and bottom–up deposition, while increased tortuosity in MT and HT hosts leads to severe concentration polarization and top-favored Li accumulation. Consequently, asymmetric cells employing the LT host demonstrated extraordinary cycling durability of 5500 h at 1C. In practical LFP full cell configurations, LT hosts preloaded with limited Li (4 mAh cm^{-2}) exhibited outstanding capacity retention (80% over 350 cycles at a low N/P ratio of 1.6). Furthermore, LT hosts paired with NCM811 cathodes under stringent conditions (N/P ratio of 0.8, E/C ratio of 2.5 g Ah^{-1}) enabled a high energy density of 398.1 Wh kg^{-1} (1516.8 Wh L^{-1}) in a double-stacked pouch-type full cell, significantly surpassing previously reported LMB systems. These findings underscore that rationally engineered host architectures combining controlled tortuosity and lithiophilicity gradients provide a highly effective strategy for mitigating dendrite formation, electrolyte decomposition, and structural instabilities inherent to Li metal anodes. Ultimately, this work provides valuable insights and a practical, scalable route for the development of stable, high-energy-density LMBs suitable for next-generation EVs and portable electronics.

Supporting Information

Supporting Information is available from the Wiley Online Library or from the author.

Acknowledgements

G.L., D.-Y.H., and S.S.P. contributed equally to this work. This work was supported by the National Research Foundation of Korea (NRF) funded by the Ministry of Science and ICT (RS-2022-NR068141) and the Korea Institute for Advancement of Technology (RS-2024-00419413).

Conflict of Interest

The authors declare no conflict of interest.

Data Availability Statement

The data that support the findings of this study are available from the corresponding author upon reasonable request.

Keywords

high-energy-density batteries, lithiophilicity gradients, lithium metal batteries, nonsolvent-induced phase separation, tortuosity-controlled hosts

Received: June 9, 2025
Revised: September 4, 2025
Published online:

[1] W. Xu, J. L. Wang, F. Ding, X. L. Chen, E. Nasybutin, Y. H. Zhang, J. G. Zhang, *Energy Environ. Sci.* **2014**, *7*, 513.
[2] X. B. Cheng, R. Zhang, C. Z. Zhao, Q. Zhang, *Chem. Rev.* **2017**, *117*, 10403.
[3] S. Li, J. Huang, Y. Cui, S. Liu, Z. Chen, W. Huang, C. Li, R. Liu, R. Fu, D. Wu, *Nat. Nanotechnol.* **2022**, *17*, 613.
[4] H. Jia, C. Zeng, H.-S. Lim, A. Simmons, Y. Zhang, M. H. Weber, M. H. Engelhard, P. Gao, C. Niu, Z. Xu, J.-G. Zhang, W. Xu, *Adv. Mater.* **2024**, *36*, 2311312.
[5] J. Ryu, D. Y. Han, D. Hong, S. Park, *Energy Storage Mater.* **2022**, *45*, 941.
[6] C. Chang, M. Zhang, Z. Lao, X. Xiao, G. Lu, H. Qu, X. Wu, H. Fu, G. Zhou, *Adv. Mater.* **2024**, *36*, 2313525.
[7] G.-X. Li, H. Jiang, R. Kou, D. Wang, A. Nguyen, M. Liao, P. Shi, A. Silver, D. Wang, *ACS Energy Lett.* **2022**, *7*, 2282.
[8] H. Zhang, G. G. Eshetu, X. Judez, C. M. Li, L. M. Rodriguez-Martínez, M. Armand, *Angew. Chem., Int. Ed.* **2018**, *57*, 15002.
[9] Y. Zhao, T. H. Zhou, L. P. H. Jeurgens, X. Kong, J. W. Choi, A. Coskun, *Chem* **2023**, *9*, 682.
[10] S. R. Chen, J. M. Zheng, D. H. Mei, K. S. Han, M. H. Engelhard, W. G. Zhao, W. Xu, J. Liu, J.-G. Zhang, *Adv. Mater.* **2018**, *30*, 1706102.
[11] X. L. Zhang, L. Ma, Y. P. Cai, J. Fransaer, Q. F. Zheng, *Matter* **2024**, *7*, 583.
[12] T. Krauskopf, F. H. Richter, W. G. Zeier, J. Janek, *Chem. Rev.* **2020**, *120*, 7745.
[13] X. B. Cheng, C. Z. Zhao, Y. X. Yao, H. Liu, Q. Zhang, *Chem* **2019**, *5*, 74.
[14] P. Bai, J. Li, F. R. Brushett, M. Z. Bazant, *Energy Environ. Sci.* **2016**, *9*, 3221.
[15] D. Y. Han, G. J. Song, S. H. Kim, S. J. Park, *Small Struct.* **2022**, *3*, 2200120.
[16] S.-H. Hong, D.-H. Jung, J.-H. Kim, Y.-H. Lee, S.-J. Cho, S. H. Joo, H.-W. Lee, K.-S. Lee, S.-Y. Lee, *Adv. Funct. Mater.* **2020**, *30*, 1908868.
[17] M. Gao, Q. Dong, M. Yao, X. Wang, J. Li, W. Zhang, H. Huang, H. Guo, Z. Sun, Q. Chen, X. Han, W. Hu, *Adv. Funct. Mater.* **2024**, *34*, 2401442.
[18] S. Niu, S.-W. Zhang, D. Li, X. Wang, X. Chen, R. Shi, N. Shen, M. Jin, X. Zhang, Q. Lian, R. Huang, A. Amini, Y. Zhao, C. Cheng, *Chem. Eng. J.* **2022**, *429*, 132156.
[19] J. Pu, J. Li, K. Zhang, T. Zhang, C. Li, H. Ma, J. Zhu, P. V. Braun, J. Lu, H. Zhang, *Nat. Commun.* **2019**, *10*, 1896.
[20] J. Jiang, D. Wang, H. Liu, K. Wu, X. Yang, Y. Shi, B. Zhao, Y. Jiang, X. Sun, J. Zhang, *Adv. Funct. Mater.* **2025**, *35*, 2417296.
[21] Y. Zhang, M. Yao, T. Wang, H. Wu, Y. Zhang, *Angew. Chem.* **2024**, *136*, 202403399.
[22] Y. Zhang, W. Luo, C. Wang, Y. Li, C. Chen, J. Song, J. Dai, E. M. Hitz, S. Xu, C. Yang, *Proc. Natl. Acad. Sci. U. S. A.* **2017**, *114*, 3584.
[23] Y. Shi, B. Li, Y. Zhang, Y. Cui, Z. Cao, Z. Du, J. Gu, K. Shen, S. Yang, *Adv. Energy Mater.* **2021**, *11*, 2003663.
[24] X. Zhu, H. Cheng, S. Lyu, J. Huang, J. Gu, Y. Guo, Y. Peng, J. Liu, C. Wang, J. Duan, S. Yang, *Adv. Energy Mater.* **2023**, *13*, 2300129.
[25] Z. Qiu, S. Shen, P. Liu, C. Li, Y. Zhong, H. Su, X. Xu, Y. Zhang, F. Cao, A. Noori, M. F. Mousavi, M. Chen, X. He, X. Xia, Y. Xia, W. Zhang, J. Tu, *Adv. Funct. Mater.* **2023**, *33*, 2214987.
[26] H. Chen, A. Pei, J. Wan, D. Lin, R. Vilá, H. Wang, D. Mackanic, H.-G. Steinrück, W. Huang, Y. Li, A. Yang, J. Xie, Y. Wu, H. Wang, Y. Cui, *Joule* **2020**, *4*, 938.
[27] G. W. Lee, Y. J. Choi, Y. H. Kim, S. G. Choi, H. S. Choi, H. K. Kim, K. B. Kim, *Carbon* **2022**, *198*, 289.
[28] Z. Zhang, L. Zhang, S. Wang, W. Chen, Y. Lei, *Polymer* **2001**, *42*, 8315.
[29] M. Yao, Q. Ruan, T. Yu, H. Zhang, S. Zhang, *Energy Storage Mater.* **2022**, *44*, 93.
[30] Y. Ma, Y. Qiu, K. Yang, S. Lv, Y. Li, X. An, G. Xiao, Z. Han, Y. Ma, L. Chen, *Energy Environ. Sci.* **2024**, *17*, 8274.
[31] C. M. Hansen, *Hansen Solubility Parameters: A User's Handbook*, 2nd ed., CRC press, Boca Raton, FL, USA, **2007**.
[32] J. Li, Y. X. Yu, P. C. Zhou, H. J. Li, Y. D. Liu, *J. Appl. Polym. Sci.* **2022**, *139*, 52383.
[33] D.-Y. Han, S. Kim, S. Nam, G. Lee, H. Bae, J. H. Kim, N.-S. Choi, G. Song, S. Park, *Adv. Sci.* **2024**, *11*, 2402156.
[34] G. R. Guillen, Y. J. Pan, M. H. Li, E. M. V. Hoek, *Ind. Eng. Chem. Res.* **2011**, *50*, 3798.
[35] I. Pastoriza-Santos, L. M. Liz-Marzán, *Nano Lett.* **2002**, *2*, 903.
[36] A. Sarkar, S. Kapoor, T. Mukherjee, *J. Phys. Chem. B* **2005**, *109*, 7698.
[37] I. Karbownik, O. Rac, M. Fiedot, P. Suchorska-Wozniak, H. Teterycz, *Eur. Polym. J.* **2015**, *69*, 385.
[38] J. Landesfeind, J. Hattendorff, A. Ehrl, W. A. Wall, H. A. Gasteiger, *J. Electrochem. Soc.* **2016**, *163*, A1373.
[39] L. S. Li, R. M. Erb, J. J. Wang, J. Wang, Y. M. Chiang, *Adv. Energy Mater.* **2019**, *9*, 1802472.
[40] J. Kang, Y. J. Song, S. Kim, D. Y. Han, J. Ryu, S. Park, *Small* **2024**, *21*, 2409114.
[41] P. Arora, Z. M. Zhang, *Chem. Rev.* **2004**, *104*, 4419.
[42] X. Liang, Q. Pang, I. R. Kochetkov, M. S. Sempere, H. Huang, X. Q. Sun, L. F. Nazar, *Nat. Energy* **2017**, *2*, 17119.
[43] Y. F. Xu, L. N. Gao, L. Shen, Q. Q. Liu, Y. Y. Zhu, Q. Liu, L. S. Li, X. Kong, Y. Lu, H. B. Wu, *Matter* **2020**, *3*, 1685.
[44] J. I. Lee, G. Song, S. Cho, D. Y. Han, S. Park, *Batteries Supercaps* **2020**, *3*, 828.
[45] S. Cho, D. Y. Kim, J.-I. Lee, J. Kang, H. Lee, G. Kim, D.-H. Seo, S. Park, *Adv. Funct. Mater.* **2022**, *32*, 2208629.
[46] C. Fang, B. Lu, G. Pawar, M. Zhang, D. Cheng, S. Chen, M. Ceja, J.-M. Doux, H. Musrock, M. Cai, B. Liaw, Y. S. Meng, *Nat. Energy* **2021**, *6*, 987.
[47] B. Lu, D. Cheng, B. Sreenarayanan, W. Li, B. Bhamwala, W. Bao, Y. S. Meng, *ACS Energy Lett.* **2023**, *8*, 3230.
[48] J. B. Park, C. Choi, S. Yu, K. Y. Chung, D. W. Kim, *Adv. Energy Mater.* **2021**, *11*, 2101544.
[49] Q. Zhang, B. Hou, X. Wu, X. Li, Z. Guo, J. Liu, D. Cao, X. Huang, J. Duan, D. Mo, J. Liu, H. Yao, *Adv. Energy Mater.* **2024**, *14*, 2401377.
[50] P. Shi, J. Ma, Y. Huang, W. Fu, S. Li, S. Wang, D. Zhang, Y.-B. He, F. Kang, *J. Mater. Chem. A* **2021**, *9*, 14344.
[51] L. X. Yuan, Z. H. Wang, W. X. Zhang, X. L. Hu, J. T. Chen, Y. H. Huang, J. B. Goodenough, *Energy Environ. Sci.* **2011**, *4*, 269.
[52] G.-R. Zhu, Q. Zhang, Q.-S. Liu, Q.-Y. Bai, Y.-Z. Quan, Y. Gao, G. Wu, Y.-Z. Wang, *Nat. Commun.* **2023**, *14*, 4617.